Combined Use of the Radar and Radiometer of TRMM to Estimate the Influence of Drop Size Distribution on Rain Retrievals

NICOLAS VILTARD

Universities Space Research Association, and NASA Goddard Space Flight Center, Greenbelt, Maryland

CHRISTIAN KUMMEROW

Laboratory for Atmospheres, Goddard Space Flight Center, Greenbelt, Maryland

WILLIAM S. OLSON

Joint Center for Earth Systems Technology, University of Maryland, Baltimore County, Baltimore, Maryland

YE HONG

Caelum Research Corporation, and NASA Goddard Space Flight Center, Greenbelt, Maryland

(Manuscript received 30 September 1999, in final form 6 July 2000)

ABSTRACT

A combination of passive microwave and radar observations from the Tropical Rainfall Measuring Mission (TRMM) satellite is used to investigate the consistency between the two sensors. Rather than relying on some absolute ''truth'' to verify retrievals, this paper focuses on one assumption—namely, the drop size distribution (DSD)—and how different DSDs lead to improved or reduced consistency. Results from a case in the central Pacific suggest that a crude consistency may be achieved if a different drop size is used for the radiometer and the radar. In this particular case, a Marshall–Palmer or a gamma distribution with the shape parameters properly set leads to similar results. Although this study offers no independent validation of its conclusions, it does demonstrate that rainfall validation need not be confined to surface rainfall measurements, which are only loosely related to the volumetric observations made by most sensors. As mean size distributions of raindrops are measured in the TRMM field experiments by disdrometers, profilers, multiparameter radars, and direct aircraft observations, the technique presented in this paper can be applied on a storm-by-storm basis, and conclusions can be verified directly.

1. Introduction

Observed radar reflectivities depend strongly upon the size of water drops. For applications such as rainfall estimation, a precise description of the drop size distribution (DSD) is therefore the key to relating the physical properties of individual droplets to the physical properties of a volume of raining atmosphere being observed. As the physical properties of droplets change with their size, it is important to know how many drops may exist for each size interval and, thus, to define an accurate DSD. Unfortunately, DSD may vary drastically in a real meteorological situation. For instance, Battan (1973) pointed out this variability by listing 69 relations between the radar reflectivity and the rain rate. Since then, many studies of DSD have been conducted, and a number of these relations have been proposed.

The Tropical Rainfall Measuring Mission (TRMM; Simpson et al. 1988) carries on the same platform the TRMM Microwave Imager (TMI) and the precipitation radar (PR). The TMI provides a measure of the brightness temperatures (hereinafter T_B) at nine frequencies: horizontal and vertical polarizations at 10, 18, 37, and 85 GHz and only vertical polarization at 21 GHz. The distance between two scans is approximately 14 km; along scan, the 85-GHz channel has a pixel every 4.5 km, and the other channels have a pixel every 9 km. This spacing leads to a swath 720 km wide with 208 pixels per scan at 85 GHz and 104 pixels per scan for the other channels. The TMI is conically scanned with a viewing angle of 49° off nadir (i.e., 52.8° incidence angle). The PR provides a measure of the vertical profile

Corresponding author address: Nicolas Viltard, CETP, 10–12 Avenue de l'Europe, 78140 Velizy, France.
E-mail: viltard@cetp.ipsl.fr

of reflectivity at 13.8 GHz, with a pixel every 4.4 km both along and cross track. The resulting swath is 220 km wide with 49 pixels per scan. The PR is cross-track scanning, $\pm 17°$ off nadir. A detailed description of the configuration of the TRMM instrument package is given in Kummerow et al. (1998).

Because the geometrical configurations of the instruments are different, the same region is sampled with an approximate time shift of 1 min. In this study, this effect will be neglected because, at the spatial scale (20 km) considered, the observed precipitation systems are nearly stationary over 1 min.

In this study, we propose to use the PR reflectivity to build a three-dimensional domain of precipitation profiles and then to use this domain as an input to a forward radiative transfer model calculation to obtain simulated brightness temperatures at the same frequencies as those of the TMI. Comparison of the observed and computed brightness temperatures will allow us to address two main points: first, the consistency of the observations from the two instruments, and second, the determination of the coarse characteristics of the DSD that leads to consistent results between the two instruments at a global scale.

Section 2 is a brief reminder of the data organization and characteristics in the framework of TRMM. Section 3 presents the methodology used to build a three-dimensional domain of precipitation using the observed PR reflectivity profiles. This section also addresses the theoretical influence of the modification of the DSD for the different algorithms. Section 4 presents basic sensitivity tests performed with a simple plane-parallel radiative transfer model. Section 5 describes the characteristics of the radiative transfer model used to perform the forward calculation of the simulated T_B. The results are presented in section 6, and the conclusions and perspectives are presented in section 7.

2. Data description

The raw data arising from the different instruments are treated through different algorithms to obtain useful TRMM products designated as ''TRMM standard data products.'' A detailed description of these products and their characteristics can be found (at the time of writing) on the Internet (http://trmm.gsfc.nasa.gov) and in Kummerow et al. (2000). We recall briefly here the main characteristics of the data used for this specific work.

We use two of these standard products, referenced as PR rain rate/PR-corrected reflectivity (2A25) and TMI brightness temperatures (1B11). Both standard products used here are version 4. All of these data are provided with corrected satellite attitude and are navigated in the latitude–longitude geographical system. The brightness temperatures are effective field-of-view T_B (Kummerow et al. 1998). The so-called corrected reflectivity is the reflectivity factor Z corrected for attenuation and bright-band effects; the associated rain rate R is obtained via a Z–R relationship. In this study, rather than using the standard 2A25 R (mm h^{-1}) we use the water content W (g m^{-3}) because it relates more directly to the brightness temperatures. The 2A25 product also gives information on the type of the observed rain (convective or stratiform) and a rain/no-rain flag.

The results of this study are based on a scene observed on a subset of orbit 3976 on 7 August 1998 from the Pacific Ocean near the equator. The choice of this subset was made to preserve homogeneity in the characteristics of the environment of the precipitating systems. The constructed three-dimensional domain consists of 335 PR scans of 49 rays. These 335 scans $\times$ 49 rays constitute a domain with dimension of 1470 km $\times$ 211 km, extending from 0- to 18-km altitude. The simulated brightness temperatures are calculated based on this domain.

3. Retrieval of the three-dimensional precipitation domain

The conversion of the measured effective reflectivity factor to water content is made through a W–Z relationship inferred from the fit of a measured dataset using Mie theory. The W–Z relationship has the form $W = aZ^b$, where a and b are weakly dependent on the temperature but depend on the shape of the assumed DSD. The W profile derived from the reflectivity profile is valid for liquid precipitation but does not apply to any of the ice-phase (see section 3b) and cloud liquid water profiles. This fact is why it is necessary to utilize a database to set the other parameters that will be needed for the forward radiative transfer calculation.

a. Choice of the DSD shape and coefficients

Of the different kinds of drop size distributions that could be used we tested two different shapes: the exponential type $N(D) = N_0 \exp(-\Lambda D)$ and the gamma type $N(D) = N_0 D^{\mu} \exp(-\Lambda D)$, where D (cm) is the drop diameter, $N(D)$ is the number density of drops with diameters between D and $D + dD$, and N_0 (m^{-4}), Λ (cm^{-1}), and μ are the shape parameters for the distribution. We will hereinafter consider the exponential type as a special case of gamma-type distribution when μ is equal to 0.

Over the past few years, an approach has been developed to compare the measured DSDs arising from different sources. This approach is known as the ''normalized DSD'' approach and was first proposed by Willis (1984). The form we are using here is described in detail in Dou et al. (1999a,b), and consists of rewriting the gamma-type equation as

$$N(D) = N_0^* \kappa(D, \mu) \exp\left[-(3.67 + \mu)\frac{D}{D_0}\right], \quad (3.1)$$

where N_0^* is the normalized N_0 and is equivalent to N_0

when μ is equal to 0. $D_0 = (3.67 + \mu)/\Lambda$ is the median volume diameter, and $\kappa(D, \mu)$ is a normalization correction factor,

$$\kappa(D, \mu) = \frac{\Gamma(4)}{3.67^4} \frac{(3.67 + \mu)^{4+\mu}}{\Gamma(4 + \mu)} \left(\frac{D}{D_0}\right)^{\mu}, \quad (3.2)$$

where Γ is the complete Gamma function. The DSD is then normalized with respect to the water content because introducing (3.2) into the definition of W leads to the following form, which is independent of μ:

$$W = 3.67^{-4}\, \Gamma(4) \pi \rho_w N_0^* D_0^4. \quad (3.3)$$

Here, ρ_w is the density of liquid water.

Using this normalized approach, it is possible to write the relationship between two integrated rainfall parameters X and Y as $X = mN_0^{*(1-n)}Y^n$, where n is independent of μ, and m is weakly dependent on μ. For instance, the fitted a coefficient of $W = aN_0^{*(1-b)}Z^b$ varies from 3.68×10^{-6} for $\mu = 0$ (exponential case) to 3.56×10^{-6} for $\mu = 4$, and the b coefficient varies from 0.56 to 0.54, respectively. The coefficients given here are obtained following Ferreira and Amayenc (1999) and Ferreira et al. (2000, unpublished manuscript, hereinafter FAOT), where N_0^* is computed by fitting the initial rain relations of 2A25 version 4 for temperatures between 273 and 293 K under the Mie assumption at 13.85 GHz. The inferred N_0^* from 2A25 for convective rain is 17.0×10^6 m^{-4}, and the inferred N_0^* for stratiform rain is 4.8×10^6 m^{-4} (hereinafter these values will be referred as $N_{0\text{orig}}^*$). These values for N_0^* are close to those found by Dou et al. (1999a), derived from airborne microphysics probe measurements made during the Tropical Ocean and Global Atmosphere Coupled Ocean–Atmosphere Response Experiment (TOGA COARE): N_0^* equal to 19.2×10^6 m^{-4} for convective rain and 3.9×10^6 m^{-4} for stratiform rain, with μ varying from 0.35 to 4.05 as a function of the rain rate (and equal to 0.99 for $10 < R < 30$ mm h^{-1}).

Because these coefficients are very weakly sensitive to the temperature, we have chosen an average relationship, valid for the range between 273 and 293 K and $\mu = 1$:

$$W = 3.069\,438 \times 10^{-6}\, N_0^{*0.455} Z^{0.545}. \quad (3.4)$$

It is possible to calculate W from Z using (3.4), but it is also possible to infer W using an alternate approach as described in Ferreira and Amayenc (1999) and FAOT using a k–W relationship (k is attenuation) that is less sensitive to calibration errors and DSD uncertainties. In Iguchi et al. (2000) and Kummerow et al. (2000) the authors concur that the standard 2A25 version 4 algorithm underestimates the rain with respect to the expected climatological values and to the other TRMM instrument retrievals. These previous studies lead us to chose a k–W power law to get a W estimate from PR that is then used in the forward radiative transfer calculation. The k–W relation leads to a rain-rate estimate that is about 20% higher than the standard estimate. In Ferreira and Amayenc (1999) and FAOT, the authors show that one can either use a k–W power law or scale the W from (3.4) (denoted W_{Std}) according to

$$W_{kW} = \varepsilon_f^{0.716} W_{\text{Std}}, \quad (3.5)$$

where W_{kW} is the W estimated from the k–W relationship, and ε_f is a standard product from 2A25 that accounts for small corrections of the initial 2A25 relations and that varies for each PR ray. This relationship is then applied in the current study to convert the k profiles given by 2A25 into water content profiles. We decided to keep this alternative W_{kW} that gives a water content slightly greater than the standard products because most of the TRMM community concurs to say that the 2A25 standard product in version 4 is underestimating the rain rate (Kummerow et al. 2000; Iguchi et al. 2000). It is then necessary to set the other atmospheric variables that are useful for the forward radiative computation through a database, as described below.

b. Database construction and profiles computation

The retrieval method is based on the Bayesian technique (or the estimated expected value method) described in Kummerow et al. (1996) and Olson et al. (1996). A database of cloud/precipitation profiles is generated from numerical cloud-resolving model simulations. In the current study, the database's cloud and precipitation profiles are generated using simulations from two different models: the Goddard Cumulus Ensemble (Tao and Simpson 1993) and the University of Wisconsin Nonhydrostatic Modeling System (Panegrossi et al. 1998). Each of the four simulations utilized has different characteristics that represent different meteorological situations. The first two simulations represent an oceanic mesoscale convective system observed on 22 February 1993 (Jorgensen et al. 1994, 1995; Olson et al. 1996, among others) during TOGA COARE. The simulation is performed at 1-km (128 km $\times$ 128 km domain) and 3-km (384 km $\times$ 384 km domain) horizontal spacings, respectively. The third simulation, performed using the University of Wisconsin model, is a thunderstorm complex observed during the Cooperative Huntsville Meteorological Experiment that is performed at 1-km spacing on a 50 km $\times$ 50 km domain. The last simulation is of Hurricane Gilbert (1988), also performed using the University of Wisconsin model at 3.3-km spacing on a domain of 205 km $\times$ 205 km. These last two simulations are described in greater detail in Panegrossi et al. (1998). The profiles are extracted at different time intervals from the simulations to sample a greater variety of situations.

In these cloud-resolving model simulations, the cloud liquid and cloud ice particles are assumed to be monodisperse (20 μm); rain, snow, and graupel have exponential-type particle size distributions based on Marshall and Palmer (1948) (MP) for rain and Rutledge and

Hobbs (1984) for snow and graupel. The density of liquid water is set to 1.0 g cm^{-3}, and the densities of snow and graupel are set to 0.1 and 0.4 g cm^{-3}, respectively.

Given a measured profile of water content retrieved from 2A25, the associated profile of atmospheric variables (vector **P**) is found in the database by

$$\mathbf{P}(\mathbf{x}) = \sum_{k\in \text{dbase}} \frac{1}{N}\mathbf{x}_k \exp\left[-\frac{0.5}{\sigma^2 M}\sum_{i=1}^{14}\eta_i^2\left(\frac{W_{\text{Obs}i}-W_{\text{Sim}ik}}{W_{\text{Obs}i}+W_{\text{Sim}ik}}\right)^2\right], \tag{3.6}$$

where $\mathbf{x}$ is the vector representing the set of variables considered in the retrieval, $\mathbf{x}_k$ is the vector of model-simulated atmospheric variables, σ is the estimated uncertainty in the 2A25 water contents, and η_i is a weight depending upon the considered atmospheric layer. The η_i are set to 0 in the ice layer (i.e., above the assumed altitude of the 0°C isotherm), and they are a maximum below the melting layer. The η_i then decrease linearly with decreasing altitude to take into account the decreasing confidence in the attenuation-corrected reflectivity and also the lack of data at the edges of the swath near the surface. The $W_{\text{Obs}i}$ and $W_{\text{Sim}ik}$ are the water content observed and obtained from the simulations, respectively, in layer *i*. The summation over *k* pertaining to dbase (dbase is the database of model simulations) represents the summation over the large ensemble of model-simulated atmospheric profiles $\mathbf{x}_k$. Here M is defined as $M = \Sigma_{i=1}^{14}\eta_i^2$, and N is also a normalization factor defined as

$$N = \sum_{k\in \text{dbase}} \exp\left[-\frac{0.5}{\sigma^2 M}\sum_{i=1}^{14}\eta_i^2\left(\frac{W_{\text{Obs}i}-W_{\text{Sim}ik}}{W_{\text{Obs}i}+W_{\text{Sim}ik}}\right)^2\right]. \tag{3.7}$$

The solution profile, expressed by (3.6), is a weighted average of all possible profiles in the model dbase: the better the agreement between $W_{\text{Obs}i}$ and $W_{\text{Sim}ik}$, the greater the weighting of profile $\mathbf{x}_k$. In the next section the quality of this adjustment is discussed.

Because the PR is able to provide information only where a rain signal exists, the problem of filling the nonprecipitating regions (i.e., below the PR detection threshold) has been solved using the TMI-observed T_B. Some description of the characteristics of the nonrainy regions is needed when taking into account the areally extensive TMI antenna patterns in the forward radiative transfer calculation. Using the TMI-observed T_B, we attempt to minimize the possible brightness temperature bias that the clear-air regions might introduce in the study. Thus, a small database of nonprecipitating atmospheric profiles with only cloud, water vapor, and temperature is generated. When a PR ray is detected as nonprecipitating (standard 2A25: rain/no-rain flag) the nonprecipitating profile that minimizes $\Sigma\,(\Delta T_B)^2$ is selected from the nonprecipitating database. The ΔT_B represents the difference between observed and simulated brightness temperatures, and the sum Σ is made over all the frequencies.

As a standard product, the PR reflectivity is given at a range resolution of 250 m along each ray. To reduce the number of levels to the 14 levels corresponding to the forward radiative transfer model calculation, a vertical filter is applied based on the Cressman (1959) technique. This filtering process allows us to diminish possible errors resulting from uncertainties in the altitude of the radar range gates and to ensure the consistency of the vertical spatial resolution between the model-simulated profiles and the radiative transfer model forward calculation.

4. Sensitivity tests

To understand the effects of beam-filling and geometry, we first performed the brightness temperature simulation using a simple radiative transfer model that is plane parallel based on Eddington's second approximation. Description of this model may be found in Weinman and Davies (1978) and Viltard et al. (1998) among many others. The forward radiative transfer model used in these sensitivity tests does not take into account the antenna pattern, and thus all the brightness temperatures are simulated at the same resolution corresponding to the radar horizontal resolution. The radiative transfer calculation is applied to one reconstructed 3D domain of precipitation derived from a subset of orbit 3976, recorded on 7 August 1998.

a. Characteristics of the 7 August 1998 scene

Figure 1 illustrates the characteristics of this scene. The domain extends approximately from 4° to 13°N and 162° to 173°W. This case presents an interesting structure extending from northeast to southwest directions, with some farther extent to the southwest to another precipitating region. The PR convective/stratiform classification shows mostly stratiform (4067 pixels) rain with spots of convection (938 pixels) embedded in the stratiform (Fig. 1b). The maximum integrated precipitating water is about 29.76 kg m^{-2}, attained in a convective region. The horizontal distribution of liquid cloud water (Fig. 1a) is well correlated with the horizontal distributions of rain and ice precipitation (Figs. 1c and 1d, respectively). The maximum precipitating water content in the first layer (0–0.5-km altitude) is 4.55 g m^{-3}, corresponding to a convective pixel. The maximum of ice is 2.03 g m^{-3} in another convective pixel, just above the 0°C isotherm. It should be noted that there is no a priori reason for the maximum ice and the maximum rain to be collocated within the same profile or pixel.

It may also be noticed on Figs. 1b–d that convective pixels generally correspond to the highest precipitation. Nevertheless, local maxima of rain may correspond to stratiform regions. This result is consistent from the

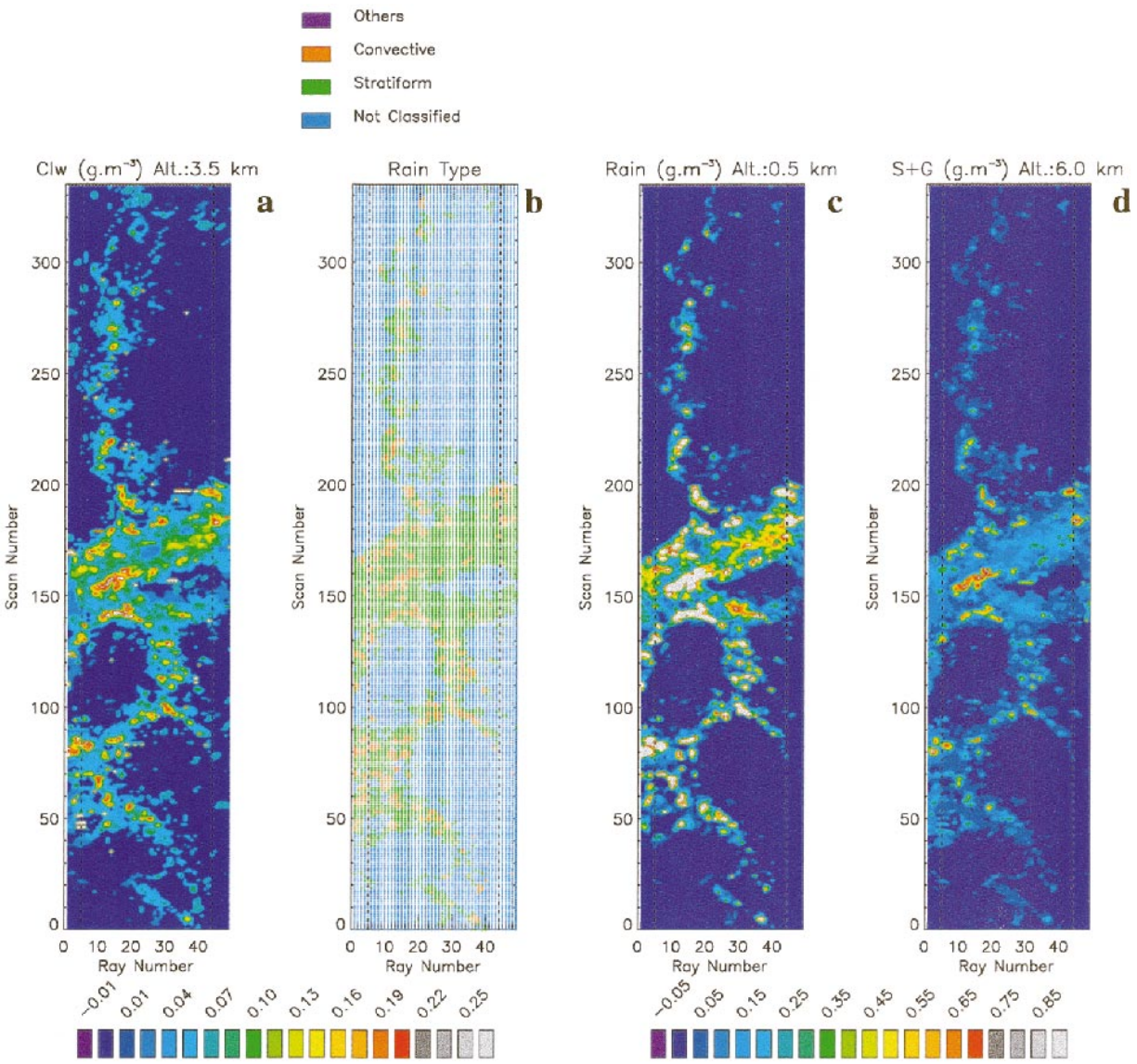

FIG. 1. Horizontal cross sections of the different species of water present in the 3D domain (scene from orbit 3976) used as an input to the radiative transfer model calculation. (a) Cloud liquid water at 3.5-km altitude; (b) convective (red)/stratiform (green) PR classification; (c) rain at 1.5-km altitude; (d) snow + graupel at 6-km altitude. All water contents are expressed in grams per meter cubed.

physics point of view but may also be an artifact from the methodology, because the differentiation between convective and stratiform profiles in the database (based on dynamics of the model) is different from the PR classification (based on both horizontal and vertical patterns of reflectivity). Nevertheless, the horizontal cross sections of the different species show good horizontal consistency despite the fact that each of the profiles has been retrieved independently from the others. Table 1 shows, for the two types of precipitation, the mean difference between the PR-calculated water content and the database-adjusted water content in grams per cubic meter (see section 3b). This table demonstrates that the observed W matches correctly the W of the profiles in the database. It is important to remember that we are using the PR-retrieved water contents to select database profiles that are actually used to set the ice-phase precipitation and other variables not directly measured by the PR. The differences between the two Ws are not negligible, but they are small enough to ensure the consistency of the ice and cloud profiles with the liquid precipitation profiles derived directly from the radar. We can also see from Table 1 that the stratiform precipitation profiles are better matched than the convective profiles because of their smoother shapes, which are better represented in the database. The convective profiles exhibit more irregular shapes with a higher variability and thus are not represented as well in the da-

TABLE 1. Mean difference between W from PR and database (see text for explanation).

Layer (km)	Stratiform	Convective
14–18	0.026	0.045
10–14	0.105	0.195
8–10	0.136	0.311
6–8	0.134	0.364
5–6	0.122	0.335
4–5	0.119	0.218
3.5–4.0	0.116	0.173
3.0–3.5	0.068	0.137
2.5–3.0	0.054	0.120
2.0–2.5	0.047	0.103
1.5–2.0	0.046	0.112
1.0–1.5	0.052	0.135
0.5–1.0	0.061	0.169
0–0.5	0.069	0.213

tabase. Table 1 gives also the distribution of the layers used in this study.

b. *Brightness temperature simulations without antenna pattern effects*

A retrieval of the rain profile structure is performed with the inferred values from 2A25, that is, $N_0^* = 17 \times 10^6$ m^{-4} for convective rain and $N_0^* = 4.8 \times 10^6$ m^{-4} for stratiform rain, using a gamma-type distribution with $\mu = 1$. The brightness temperature forward calculation is performed using the corresponding Mie coefficients computed for the two different N_0^*. This sensitivity study allows us to understand the variations of the computed T_B for individual profiles. Figure 2 illustrates the differences of radiometric signatures between the two rain regimes. It can be seen that, depending on the frequency, the result varies. First, at 10 GHz the saturation regime (defined as the regime in which scattering balances emission, leading to a quasi-constant T_B as W increases) is not attained (Figs. 2a,b). Because of the difference in N_0^*, the convective rain profiles always yield lower brightness temperatures than do the stratiform rain profiles having the same total integrated water content. This result is from the poor absorption efficiency of the smaller drops for which the proportion increases dramatically as N_0^* increases. Second, for intermediate frequencies such as 19, 21, and 37 GHz (Figs. 2d–g), similar behavior is observed as long as the total water content remains below the saturation value. The saturation value depends on the considered frequency and on the chosen N_0^*: approximately 7 kg m^{-2} (10 kg m^{-2}) at 19 GHz, 5 kg m^{-2} (7 kg m^{-2}) at 21 GHz, and 4 kg m^{-2} (5 kg m^{-2}) at 37 GHz for stratiform (convective) rain. On the other hand, above the saturation value, the brightness temperature tends to increase as N_0^* increases. This result is due to the greater proportion of larger drops as the rain rate increases that compensate for the effect of the N_0^* increase. The total absorption efficiency is higher, even with the contribution from scattering. Third, the highest frequency (Figs. 2h,i) is always saturated, and its behavior is similar to the saturated regime of the intermediate frequencies. However, this reason is not so obvious from Fig. 2, because the DSD is set to a constant value for the ice phase in this study.

5. Brightness temperature forward calculations

For a precise comparison between the ''PR-derived'' brightness temperatures and the TMI-observed brightness temperatures, a more complex forward radiative transfer model is used, derived from the previously mentioned version. The T_B emerging from the top of the atmosphere are calculated using a repeated application of the one-dimensional version of Eddington's second approximation (Weinman and Davies 1978). All radiance slant paths through the three-dimensional domain are considered independently. The antenna pattern for each frequency is approximated by a Gaussian weighting function with the same 3-dB beamwidth as the actual antenna pattern (Kummerow et al. 1998). The upwelling microwave radiances over ocean depend on the sea surface characteristics and the atmospheric constituents. In this study, the sea surface temperature is assumed to be 300 K, the salinity is set to a constant value of 35 ppm, and the foam coverage induced by wind-driven waves is taken into account in relation to the surface wind speed (Wilheit 1979).

Gaseous absorption follows the approach of Liebe (1985) and takes into account both water vapor and molecular oxygen. The cloud water DSD follows the empirical formula given in Liou (1992), and the cloud ice distribution is based on the work of Heymsfield and Platt (1984). These nonprecipitating particles are small enough with respect to the TMI channel wavelengths to be treated in the Rayleigh approximation. The precipitating particles are assumed to be spherical, and Mie theory is applied to compute their respective extinction coefficient, single-scatter albedo, and asymmetry factor.

In the interpretation of the results to follow, a classification of the pixels into stratiform and convective categories has been necessary at some ''characteristic'' TMI resolution that is theoretically frequency dependent. Because of the difference in resolution and angle of view of the two instruments, this classification may differ from the PR classification. Previously, we retained the PR classification set in 2A25, but for the statistical results to be presented in section 6 a classification for the TMI pixels has been established on the basis of the PR classification: the average trend given by all the PR pixels included in a 37-GHz TMI pixel (18 km $\times$ 25 km) determines the class of the corresponding TMI pixel. In other words, if more than 50% of the PR pixels within a 37-GHz pixel are classified as convective, then the TMI pixel is considered to be convective, otherwise it is classified as stratiform. The difference in sensor resolution is expected to have a greater effect for con-

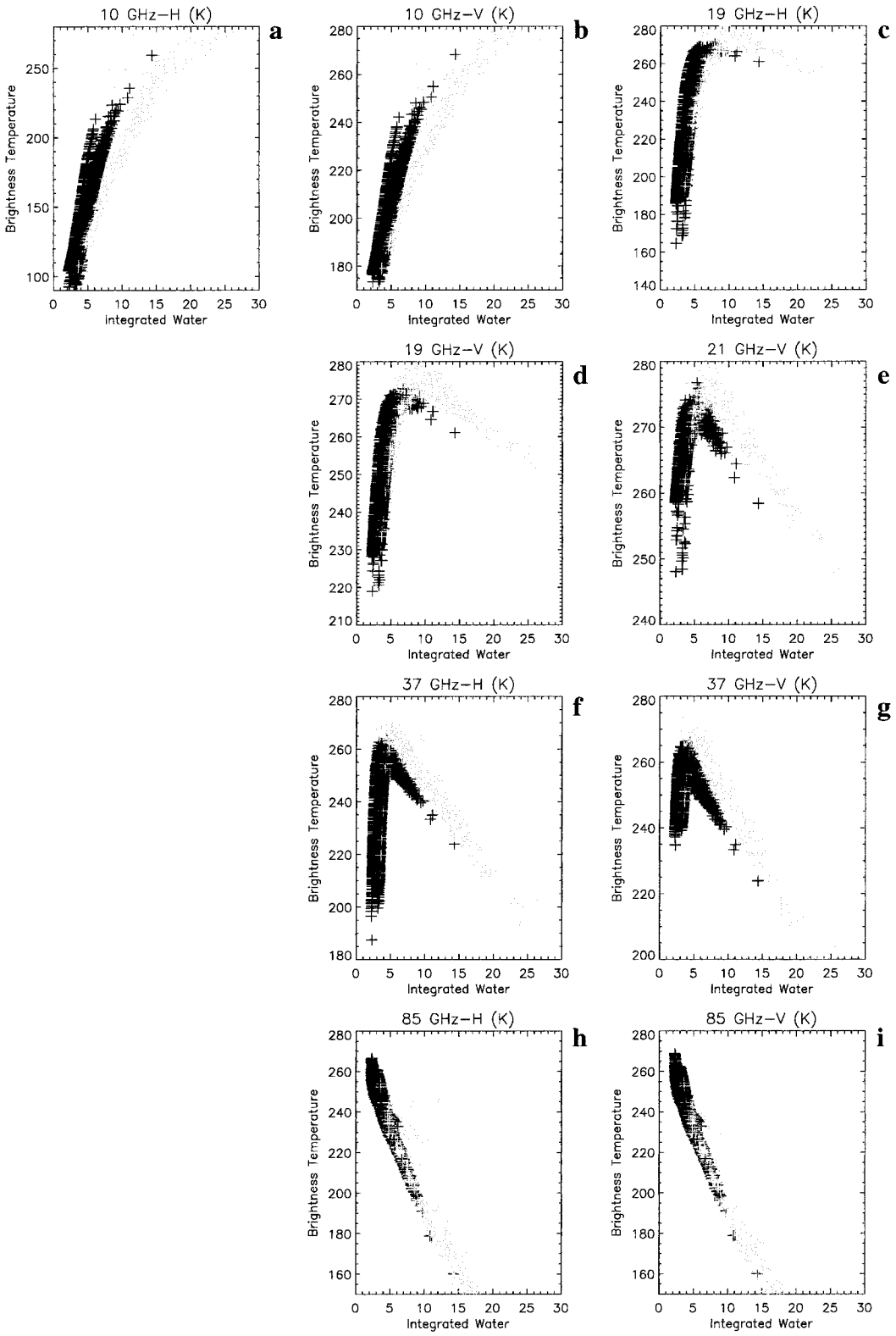

FIG. 2. Relation between computed brightness temperature (K) and integrated water content (kg m^{-2}) for two different N_0^* values equal to 4.8×10^6 (dark gray) and 17×10^6 m^{-4} (light gray) for the scene extracted from orbit 3976. These two values for N_0^* correspond, respectively, to $N_{0\text{orig}}^*$ for stratiform and convective rain. Images (a)–(i) correspond, respectively, to the nine TRMM frequencies: 10-H, 10-V, 19-H, 19-V, 21-V, 37-H, 37-V, 85-H, and 85-V. No antenna pattern is taken into account in the brightness temperature simulation.

vective regions because of the greater mixture of precipitation types observed in these regions.

The lower resolution of the TMI brings about some modification of the characteristics of the observed system. Once reduced to the TMI resolution, the number of convective pixels becomes 172 and the number of stratiform pixels becomes 1568. The maximum integrated precipitating water is reduced to 21.9 kg m^{-2}. The maximum precipitating water content in the lowest layer is 3.76 g m^{-3} corresponding to a stratiform pixel adjacent to a convective region. The maximum equivalent water content of ice is 2.26 g m^{-3}, which is attained in a convective pixel. This result demonstrates how the TMI resolution might present a problem for retrieval techniques, especially in the less homogeneous convective rain regions.

6. Results

The forward radiative computation is performed using five different assumed DSDs: one exponential-type DSD with MP values for both N_0^* stratiform and convective (8×10^6 m^{-4}), and 4 gamma-type DSDs with a scaling of the original PR N_0^* (see section 3a; the ratio between stratiform and convective N_0^* remains the same all the time). The scaled cases are half $N_{0\text{orig}}^*$, twice $N_{0\text{orig}}^*$, and 3 times $N_{0\text{orig}}^*$ (hereinafter $0.5N_{0\text{orig}}^*$, $2N_{0\text{orig}}^*$, and $3N_{0\text{orig}}^*$, respectively).

a. Simulated TB for the original N_0^*

Figure 3 illustrates the brightness temperature simulations that the antenna pattern affects. The T_B computation is performed using an original N_0^* equal to $N_{0\text{orig}}^*$ (see section 3a), that is, a convective N_0^* approximately 3.5 times the stratiform N_0^*. One may notice that the agreement is generally good between the observed and simulated brightness temperatures. The general spatial patterns are very well reproduced at each frequency; the main differences arise when considering the intensities of the computed T_B as compared with the observed. The first obvious feature is the lack of emission at 10 GHz-V (Figs. 3a,b). The background brightness temperature is correctly simulated, but the maximum in rain is 233.8 K in the observations and only 231.5 K in the simulation. At 10 GHz-H (not shown), the respective maxima are 200.6 K in the observations but only 196.0 K in the simulation. One can see that this difference is less important at 19 GHz-V (Figs. 3c,d) for which the regions of maximum emission are similar in shape. The observed maximum is 272.1 K, and the computed maximum is only 269.7 K (for 19 GHz-H, the maxima are respectively 268.5 and 266.4 K). Both simulated and observed 21-GHz-V results exhibit the same kinds of features. Their respective maxima are 274.8 K for the observation and 272.7 K for the simulation. Note that in the region of strong convection some saturation may occur (scan numbers 60–63; ray numbers 82–98). The comparison between the observed and computed 37-GHz results is more critical, mostly because of the lack of information regarding ice precipitation provided by the radar. The PR appears to be poorly sensitive to ice, which makes the restitution of the profiles above the 0°C isotherm somehow harder to validate. We also know that one of the weaknesses of our database of model-simulated profiles is the proper description of the ice-phase microphysics. This weakness is why, even if the main emission patterns are still reproduced, the 37-GHz-V field (Figs. 3g,h) exhibits strong evidence of scattering by ice in the simulated T_B that does not appear in the observed T_B. These effects are primarily confined to regions classified as convective by the radar. In the vertical polarization, the observed maximum is 274.5 K as compared with the computed maximum of 268.5 K. The observed maximum is 269.1 K and the computed maximum is 263.0 K at 37 GHz-H. Last, the 85-GHz T_B simulation is even more affected by the ice-scattering problem. It is clear that the simulated 3D domain has too much ice in its upper layers, leading to a general low bias in 85-GHz T_B for both polarizations. The minimum observed T_B at 85 GHz-V is 286.4 K, and the minimum observed T_B at 85 GHz-H is 284.3 K; the minimum computed T_Bs are 288.5 and 286.4 K, respectively, for V and H polarizations.

b. Simulation with different N_0^*

In this section, we examine the effect of the DSD on the simulated brightness temperatures, given a domain of water profiles derived from the radar. It should be emphasized that, even if we vary the N_0^* in the forward radiative transfer calculation, the three-dimensional domains of hydrometeor water contents described above are unchanged. Thus, interpretation of the results should be always considered with respect to the T_Bs simulated and described in the previous section that were based on $N_{0\text{orig}}^*$.

Table 2 presents the average brightness temperatures obtained for the stratiform type of rain and for the different DSDs considered. The ''MP'' refers to an exponential-type distribution with $N_0^* = 8 \times 10^6$ m^{-4} for both convective and stratiform pixels (for exponential distribution, the N_0^* identifies with the classic N_0). The other distributions are the gamma type with μ equal to 1 and the N_0^* eventually scaled but keeping the ratio between the N_0^* convective and N_0^* stratiform (e.g., $0.5N_{0\text{orig}}^*$ has an $N_0^* = 2.4 \times 10^6$ m^{-4} for stratiform rain and 8.5×10^6 m^{-4} for convective rain). The first thing to note from Table 2 is the decreasing sensitivity of T_B to changes in N_0^* as the frequency increases. The 21-GHz case is special, because this channel is mostly sensitive to the water vapor and cloud water and thus is not affected by DSD changes. It is also clear that the average brightness temperature for the lower channels decreases as N_0^* increases. These results are consistent with the test presented in section 4b. We can see how

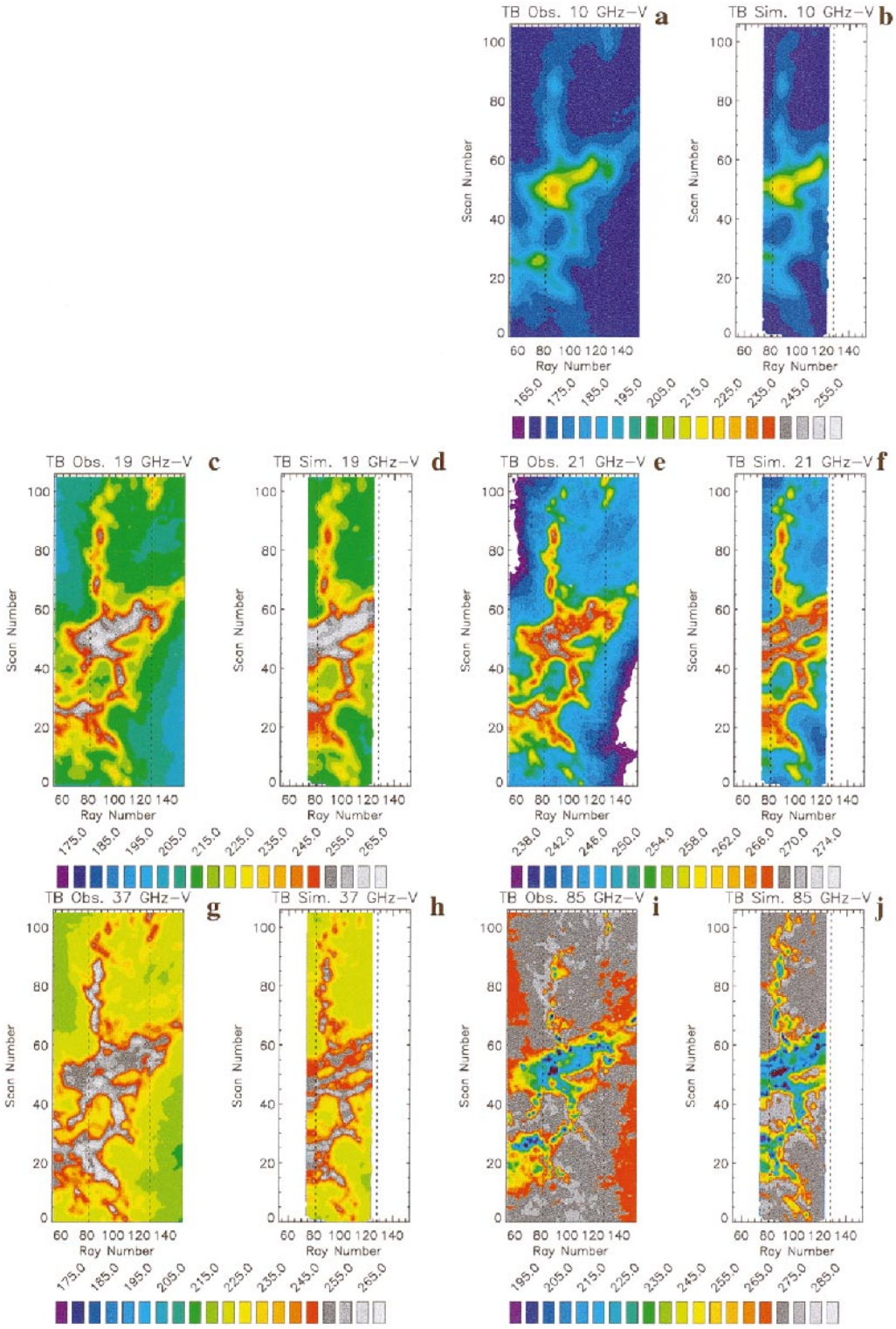

FIG. 3. Observed brightness temperatures for (a) 10 GHz V, (c) 19 GHz-V, (e) 21 GHz-V, (g) 37 GHz-V, and (i) 85 GHz-V vs computed brightness temperatures obtained from the 3D domain of Fig. 2 [(b) 10 GHz V, (d) 19 GHz-V, (f) 21 GHz-V, (h) 37 GHz-V, and (j) 85 GHz-V]. All T_Bs are expressed in kelvin.

TABLE 2. Mean brightness temperature at different frequencies and polarizations for stratiform rain type (1578 pixels) for five different DSDs as compared with the observations. See text for further explanation.

Stratiform	10-H	10-V	19-H	19-V	21-V	37-H	37-V	85-H	85-V
MP	134.2	195.2	224.7	249.3	265.5	241.2	254.1	238.8	239.4
$0.5N^*_{0\text{orig}}$	141.4	199.4	227.9	250.3	265.1	240.3	251.9	238.4	238.9
$N^*_{0\text{orig}}$	134.5	195.4	225.7	249.7	265.5	240.8	253.2	238.1	238.6
$2N^*_{0\text{orig}}$	128.8	192.0	223.0	248.7	265.7	241.9	255.2	239.2	239.8
$3N^*_{0\text{orig}}$	126.1	190.5	221.1	247.8	265.6	242.0	255.9	239.6	240.2
Observations	135.9	197.0	221.9	247.1	263.8	242.5	257.3	244.7	250.8

the variation of the number of the biggest drops, with high-absorption efficiencies, affects the so-called emissivity channels. The trend at 85 GHz is reverse, because this channel's radiance is mostly due to ice scattering. It is important to note also that the MP case is very close to the $N^*_{0\text{orig}}$ case. This suggests that the MP case could be a good approximation of the DSD at low spatial resolution (1ow-frequency channels) and for stratiform rain.

Table 3 is the same as Table 2, but for convective rain. The same general trends appear for convective rain and stratiform rain; nevertheless, it may be noted that the average T_Bs for convective rain (both simulated and observed) are smaller than the average T_Bs for stratiform rain. For this particular scene, the difference appears to be small, but tests performed on other scenes confirm this tendency. This result is consistent with the remark made in section 4b. On the other hand, the average observed 85-GHz T_Bs (both polarizations) are clearly lower in convective rain than in stratiform rain, which seems to be consistent with the idea of higher ice density or concentration in regions of strong updrafts. Greater scattering in the convective regions appears to be represented in the cloud-model simulations, because the simulated 85-GHz T_Bs exhibit the same feature as the observed T_Bs. It may be noted that, in a rain retrieval algorithm, the convective and stratiform rain might be difficult to distinguish because of the combined effects of both high spatial heterogeneity of convection and the possibly higher N^*_0 of the convective rain DSD.

Presented in Table 4 are the root-mean-square (rms) differences between the observed and simulated T_Bs; in Table 5 the variances of the rms differences are listed. The variances are on the same order of magnitude as the rms difference itself for each channel, which indicates the high variability of the quality of the simulation from one pixel to another. On the other hand, the rms difference is less than 8 K for all of the emissivity channels and about 15 K at 85 GHz. This range represents an error of less than 10% between the simulated and the observed T_B.

Another interesting feature is the apparent frequency dependence of the best fit between the observed and simulated T_Bs. At 10 GHz, it seems that the best fit is obtained using the MP DSD or the $N^*_{0\text{orig}}$. However, at the higher-frequency channels, a higher N^*_0 is required. One may note also that the best fit is obtained using $2N^*_{0\text{orig}}$ for the horizontal polarization of 19 and 37 GHz, but the best fit is obtained using $3N^*_{0\text{orig}}$ for the vertical polarization of 19, 21, and 37 GHz. This result might be an indication of biased surface modeling in the radiative transfer simulations of this study. The variances do not show this polarization-dependent feature, but it is clear that the smallest variances (except for the 10-GHz channel) are always obtained using the 2- or $3N^*_{0\text{orig}}$ case. This apparent need for different N^*_0 for different channels could also be due to the fact that different N^*_0 were assumed in 2A25 and the forward radiative transfer calculations. Future studies will investigate this particular point.

7. Conclusions and perspectives

In this study, PR reflectivity profiles are used to build a three-dimensional domain of precipitation similar to those that can be produced by a cloud model. The domain is then used as input to a radiative transfer model to calculate the brightness temperatures emerging from the top of the atmosphere. The computed T_Bs are then compared with the T_Bs actually observed by the TMI. Throughout the different steps of the process it is possible to use different values for N_0, the intercept parameter of the DSD, looking for the value that gives the best statistical agreement between the observed and

TABLE 3. Same as Table 2, but for convective rain type (162 pixels).

Convective	10-H	10-V	19-H	19-V	21-V	37-H	37-V	85-H	85-V
MP	134.2	195.5	227.9	250.7	265.4	242.8	253.2	236.5	236.9
$0.5N^*_{0\text{orig}}$	138.3	197.9	229.7	251.3	265.2	242.1	252.1	236.3	236.7
$N^*_{0\text{orig}}$	132.2	194.4	227.7	250.7	265.4	242.4	252.8	235.8	236.2
$2N^*_{0\text{orig}}$	127.1	191.4	225.6	250.1	266.1	244.4	255.6	237.3	237.8
$3N^*_{0\text{orig}}$	124.6	189.9	224.0	249.4	266.0	244.7	256.3	237.8	238.3
Observations	134.9	196.6	223.3	247.9	264.1	241.5	256.2	241.0	246.0

TABLE 4. Root-mean-square (rms) difference between simulated and observed T_B for 1740 pixels. Boldface indicates the smallest values.

	10-H	10-V	19-H	19-V	21-V	37-H	37-V	85-H	85-V
MP	**5.23**	**2.90**	6.22	3.74	2.57	7.54	5.25	13.95	15.93
$0.5N^*_{0\text{orig}}$	7.54	4.02	7.62	4.20	2.58	7.82	6.69	14.06	16.15
$N^*_{0\text{orig}}$	5.56	3.27	6.59	3.87	2.54	7.59	5.87	14.27	16.40
$2N^*_{0\text{orig}}$	8.63	5.39	**5.98**	3.52	2.53	**7.53**	4.58	13.82	15.71
$3N^*_{0\text{orig}}$	10.76	6.78	6.11	**3.39**	**2.48**	7.86	**4.53**	**13.74**	**15.51**

TABLE 5. Variance of the rms difference between simulated and observed T_B. Boldface indicates the smallest values.

W_{kW}	10-H	10-V	19-H	19-V	21-V	37-H	37-V	85-H	85-V
MP	**4.56**	**2.44**	5.56	3.15	1.87	7.33	4.29	11.55	13.02
$0.5N^*_{0\text{orig}}$	6.05	3.37	6.51	3.57	1.93	**7.00**	4.42	11.63	13.11
$N^*_{0\text{orig}}$	4.78	2.60	5.81	3.29	1.91	7.32	4.52	12.00	13.50
$2N^*_{0\text{orig}}$	6.60	3.63	5.35	3.03	1.86	7.40	4.08	11.39	12.84
$3N^*_{0\text{orig}}$	7.96	4.34	**5.27**	**2.92**	**1.84**	7.39	**4.05**	**11.30**	**12.73**

computed T_Bs. Here, we tested both exponential-type and gamma-type DSDs, using the formalism of the normalized DSDs. In the normalized DSD approach, the classic N_0 is substituted by N_0^*. The N_0^* and N_0 are equal for the exponential-type distribution.

On the one hand, the structures and the mean intensity of the computed brightness temperatures are very close to the observations: the average difference is roughly 8–10 K, which represents an error below 5%. On the other hand, the errors are not uniform for all the channels. A good value on a statistical basis would be 2 or 3 times the $N^*_{0\text{orig}}$, if one looks for a global agreement regardless of the kind of precipitation. Because this study has been conducted only for one scene, it is difficult draw any conclusion for the convective and stratiform rain types separately. Nevertheless, both appear to require higher N_0^* values in the radiative transfer computation as compared with the radar retrieval. The 10-GHz channel is somewhat anomalous, however, requiring an N_0^* value equal to the classic Marshall–Palmer value or to $N^*_{0\text{orig}}$. These results should not be regarded as contradictory to what may be found from gauges or other in situ measurements. One has to remember that the radiometric signals are integrated over very large areas, and the local characteristics of the DSD may vary considerably. Furthermore, the suggested values for N_0^* may yield the best agreement by compensating for some other effects described below, and so these values may not necessarily be correct from the perspective of rain microphysics.

The TRMM algorithms are constantly evolving to produce, it is hoped, a better and better estimate of the rain. The current study should be viewed more as a presentation of methodology rather than as a presentation of final results. More tests are necessary over a greater number of meteorological situations.

It is nevertheless obvious that some important problems need to be addressed. The maximum computed T_Bs are globally too low at 10 GHz. Different effects probably acting altogether might be considered, such as the emission contribution from light rain (under the sensitivity of the PR), the high sensitivity of this channel to near-surface rain rate where the PR is not necessarily the most accurate, and the effect of the bright band on the radiometric signal. The ice phase is also very difficult to adjust because of the weak sensitivity of the PR to ice-phase precipitation and the general lack of knowledge regarding ice-phase microphysics. Once these difficulties are addressed, the methods described here may lead to a better understanding of the rain drop size distribution and its characteristics on spatial scales from a few kilometers to a few tens of kilometers. In the future, it might be possible to build a database of ''solution'' profiles for a TMI retrieval method based on observed data collected at the resolution of the PR, eliminating a possible bias stemming from the limited number of model simulations available.

Acknowledgments. The authors thank Toshio Iguchi (CRL) and Paul Amayenc (CETP) for their great help in explaining the PR algorithm's principles and tricks. They also thank the helpful reviewers for their comments. This work has been conducted under the USRA/Goddard Visiting Scientist Program.

REFERENCES

Battan, L., 1973: *Radar Observations of the Atmosphere*. University of Chicago Press, 323 pp.

Cressman, G. W., 1959: An operational objective analysis system. *Mon. Wea. Rev.*, **87,** 367–374.

Dou, X., J. Testud, P. Amayenc, and R. Black, 1999a: The parameterization of rain for a weather radar. *C. R. Acad. Sci. Earth Planet. Sci.*, **328,** 577–582.

——, ——, ——, and ——, 1999b: The concept of normalized gamma distribution to describe raindrop spectra, and its use to parameterize rain relations. Preprints, *29th Int. Conf. on Radar Meteorology*, Montreal, Quebec, Canada, Amer. Meteor. Soc., 625–628.

Ferreira, F., and P. Amayenc, 1999: Impact of adjusting rain relations on rain profiling estimates from the TRMM precipitation radar. Preprints, *29th Int. Conf. on Radar Meteorology*, Montreal, Quebec, Canada, Amer. Meteor. Soc., 643–646.

Heymsfield, A. J., and C. M. R. Platt, 1984: A parameterization of the particle size spectrum of ice clouds in terms of the ambient temperature and ice water content. *J. Atmos. Sci.*, **41,** 846–855.

Iguchi, T., T. Kozu, R. Meneghini, J. Awaka, and K. Okamoto, 2000: Rain-profiling algorithm for the TRMM precipitation radar. *J. Appl. Meteor.*, **39,** 2038–2052.

Jorgensen, D. P., T. J. Matejka, D. Johnson, and M. A. LeMone, 1994: A TOGA/COARE squall line seen by multiple airborne Doppler radars. Preprints, *Sixth Conf. on Mesoscale Processes*, Portland, OR, Amer. Meteor. Soc., 25–28.

——, ——, and M. A. LeMone, 1995: Structure and momentum fluxes within a TOGA/COARE squall line system observed by airborne Doppler radar. Preprints, *21st Conf. on Hurricanes and Tropical Meteorology*, Miami, FL, Amer. Meteor. Soc., 579–581.

Kummerow, C., B. S. Olson, and L. Giglio, 1996: A simplified scheme for obtaining precipitation and vertical hydrometeor profiles

from passive microwave sensors. *IEEE. Trans. Geosci. Remote Sens.,* **34,** 1213–1232.

——, W. Barnes, T. Kozu, J. Shiue, and J. Simpson, 1998: The Tropical Rainfall Measuring Mission (TRMM) sensor package. *J. Atmos. Oceanic Technol.,* **15,** 809–817.

——, and Coauthors, 2000: The status of the Tropical Rainfall Measuring Mission (TRMM) after two years in orbit. *J. Appl. Meteor.,* **39,** 1965–1982.

Liebe, H. J., 1985: An updated model for millimeter wave propagation in moist air. *Radio. Sci.,* **20,** 1069–1089.

Liou, K. N., 1992: *Radiation and Cloud Processes in the Atmosphere: Theory, Observation and Modeling.* Oxford University Press, 487 pp.

Marshall, J. S., and W. M. Palmer, 1948: The distribution of raindrops with size. *J. Meteor.,* **5,** 165–166.

Olson, W. S., C. D. Kummerow, G. M. Heymsfield, and L. Giglio, 1996: A method for combined passive–active microwave retrievals of clouds and precipitation profiles. *J. Appl. Meteor.,* **35,** 1763–1789.

Panegrossi, G., and Coauthors, 1998: Use of cloud model microphysics for passive microwave-based precipitation retrieval: Significance of consistency between model and measurement manifolds. *J. Atmos. Sci.,* **55,** 1644–1673.

Rutledge, S. A., and P. V. Hobbs, 1984: The mesoscale and microscale structure and organization of clouds and precipitation in midlatitude cyclones. XII: A diagnostic modeling study of precipitation development in narrow cold-frontal rainbands. *J. Atmos. Sci.,* **41,** 2949–2972.

Simpson, J., R. F. Adler, and G. R. North, 1988: A proposed Tropical Rainfall Measuring Mission (TRMM) satellite. *Bull. Amer. Meteor. Soc.,* **69,** 278–295.

Tao, W. K., and J. Simpson, 1993: Goddard Cumulus Ensemble model. Part I: model description. *Terr. Atmos. Oceanic Sci.,* **4,** 35–72.

Viltard, N., E. Obligis, V. Marécal, and C. Klapisz, 1998: Retrieval of precipitation from microwave airborne sensors during TOGA COARE. *J. Appl. Meteor.,* **37,** 701–717.

Weinman, J. A., and R. Davies, 1978: Thermal microwave radiances from horizontally finite clouds of hydrometeors. *J. Geophys. Res.,* **83,** 3099–3107.

Wilheit, T. T., 1979: A model for the microwave emissivity of the ocean's surface as a function of wind speed. *IEEE Trans. Geosci. Electron.,* **GE-17,** 244–249.

Willis, P. T., 1984: Functional fits to some observed drop size distributions and parameterization of rain. *J. Atmos. Sci.,* **41,** 1648–1661.